Effect of telescope alignment on a stellar interferometer

Irene L. Porro, Wesley A. Traub, and Nathaniel P. Carleton

For a ground-based stellar interferometer, we investigate the effect of wave-front distortions that are due to telescope alignment errors and other factors. We apply the results to the IR/Optical Telescope Array (IOTA) interferometer. We present the computational method used in our simulation program to calculate explicitly the wave-front shape from an arbitrarily misaligned telescope. We calculate the wave-front shape and variance for a suite of misalignment conditions and interpret these results to find allowable tolerances on the positions and tilts of the telescope mirrors. We calculate the expected Strehl ratios from a total of ten types of factor, including telescope alignment, that are expected to be important in a real interferometer. Ranking the expected wave-front perturbations, we find that three of them, the wave-front curvature from atmospheric turbulence, the servo system time constant, and the flatness of the relay optics surfaces, are more significant than the telescope alignment factor. We compare observational experience at IOTA with our model estimate of the overall Strehl ratio in the visual and the infrared, finding moderately good agreement and, more important, a guide for future instrumental improvements.

OCIS code: 350.1260.

1. Introduction: Visibility and Strehl Ratio

In a Michelson stellar interferometer the measured visibility of the interference fringes V_{meas} is related to the intrinsic visibility of the object V_{obj} by a product of two factors that describe the degradation of modulation that is due to the atmosphere and to the instrument, respectively. The instrument factor can in turn be decomposed into a series of factors, each of which represents essentially a different subsystem of the interferometer.

This approach is, of course, only an approximation to reality, inasmuch as we assume that the various factors are independent and multiplicative in their effects on the amplitude of interference fringes. Inasmuch our interest here is in small departures from the ideal, the particular mathematical form that we use to describe each factor is not important, because for a particular small perturbation all representations will have approximately the same Taylor series expansion. We therefore choose to describe these factors in terms of Strehl ratios.

If we can estimate the wave-front perturbation in terms of an optical path root-mean-square (rms) departure from the ideal, the Strehl ratio is given by the approximate relation

$$S \simeq \exp(-\sigma^2), \tag{1}$$

where $\sigma = 2\pi\delta/\lambda$ is the phase rms and δ is the optical path rms across the wave front. It was shown by Mahajan[1] that this approximation gives the Strehl ratio with less than 10% error as long as $S \geq 0.3$. If the visibility is affected by a mechanism other than a wave-front perturbation, we shall still describe it in terms of a Strehl ratio, for the purpose of keeping the terminology consistent.

With these assumptions, we write the observed fringe visibility as

$$V_{\mathrm{meas}} = S_{\mathrm{atm}} S_{\mathrm{inst}} V_{\mathrm{obj}}, \tag{2}$$

where S_{atm} is the Strehl ratio associated with the wave-front perturbation that is due to the atmosphere and S_{inst} is Strehl ratio associated with the instrument. Each of these quantities is real and in the range [0, 1].

For a two-beam Michelson stellar interferometer it can be shown[2] that the variance of the combined wave front is given by the variance of a single aperture's wave front, if terms of order σ^3 and higher are neglected; we note that this is true only if there is no

When this work was performed, all the authors were with the Harvard-Smithsonian Center for Astrophysics, 60 Garden Street, Cambridge, Massachusetts 02138. I. L. Porro (porro@mpia-hd.mpg.de) is now with the Max-Planck-Institut für Astronomie, Königstuhl 17, 69117 Heidelberg, Germany.

Received 26 March 1999; revised manuscript received 17 June 1999.

0003-6935/99/286055-13$15.00/0

spatial correlation between the combined wave fronts.

We write the overall instrument Strehl ratio S_{inst} as the product of nine Strehl ratios:

$$S_{\text{inst}} = S_{\text{servo}} S_{\text{flat}} S_{\text{align}} S_{\text{diff}} S_{\text{flux}} S_{\text{over}} S_{\text{vib}} S_{\text{win}} S_{\text{pol}}. \quad (3)$$

Then, including S_{atm}, the brief meaning of each term is as follows: S_{atm}, wave-front curvature from atmospheric turbulence; S_{servo}, star-tracker servo system time constant; S_{flat}, surface flatness or deviations of the optical components; S_{align}, wave-front distortion owing to telescope misalignment; S_{diff}, diffraction in the relayed beams; S_{flux}, flux imbalance at the combined beams; S_{over}, star image constant overlap error; S_{vib}, mechanical vibration in the optical path; S_{win}, index-of-refraction inhomogeneities in windows; and S_{pol}, polarization effects.

In this paper we focus on S_{align} because the telescope alignment is largely under the control of the observer and, in principle, can be made essentially perfect. In particular we analyze the IR/Optical Telescope Array (IOTA) system,[3–5] in which the light collectors consist of a siderostat followed by an afocal Cassegrain beam compressor.

We discuss the telescope alignment procedure in Section 2, the simulation program in Section 3, simulation results as a guide to alignment in Section 4, alignment tolerances in Section 5, expected Strehl ratios from each type of perturbation in Section 6, and a comparison with observations in Section 7.

2. Alignment Procedure

The IOTA interferometer has been described elsewhere, but the parts of the description that are relevant to optical alignment are briefly recapitulated here. The interferometer has two arms arranged in an L shape, with a long arm of length 35 m oriented approximately northeast and a short arm of length 15 m at right angles toward the southeast. There are 17 stations along these arms, at intervals of 5 and 7 m, at which points movable telescopes may be placed. The IOTA system originally had two telescopes, and a third was added in 1999.

Each Mersonne telescope has a concave paraboloidal primary mirror (effective diameter, 0.45 m; blank diameter, 0.4572 m), a convex paraboloidal secondary mirror, an afocal Cassegrain configuration, a primary focal ratio of $f\# = 2.5$, and a beam reduction factor of $m = 0.10$. The magnitudes of the primary and the secondary focal lengths are $f_p = 1.143$ m and $f_s = 0.1143$ m, respectively, and their spacing is $f_p - f_s$. Thus the output beam is parallel and compressed by a factor of 10.

Each telescope is stationary, pointing east in azimuth and down from the horizontal by an angle of 30°. A computer-controlled, steerable siderostat flat mirror feeds starlight to the telescope; in autocollimation mode, the siderostat can also be oriented perpendicular to the telescope axis. The roll axis of the siderostat is mechanically fixed to be nominally coincident with the intended mechanical axis of the telescope; the tilt axis intersects the roll axis, is perpendicular to it, and is carried by the roll action, so during star tracking it is not fixed in space. The tilt axis lies in the plane of the siderostat mirror, to mechanical assembly tolerance.

A. Geometric Alignment

The geometric alignment procedure of the siderostat-telescope system is as follows: The secondary mirror and its support mechanism are removed, so there is no obstruction between the primary mirror and the siderostat flat. A precision alignment telescope is centered in the central hole of the primary mirror's support structure, and it is pointed toward the nominal two-axis rotation center of the siderostat mirror's surface, roughly 2.25 m distant. The siderostat mirror is rotated about the roll axis, and, if the reflected line of sight moves, the tilt is adjusted and the process is iterated until there is no apparent change in reflection angle. This procedure makes the alignment telescope parallel to the rotation axis and defines the symmetry axis to which the primary and the secondary mirrors are to be adjusted.

The outer perimeter of the primary is mechanically centered to the alignment axis. One adjusts the tilt of the primary by placing an illuminated pinhole on the alignment axis at a distance of approximately $2f_p$ from the primary vertex, viewing the reflection of the pinhole via the primary and the siderostat, and tilting the primary until the reflected image coincides with the illuminating object. (In practice, the center of curvature falls a few centimeters beyond the surface of the siderostat mirror, so the object is placed a few centimeters above the mirror, and both the object and its image are viewed in reflection via this mirror.) This action makes the primary paraboloid axis coincident with the alignment and the roll axes, to within geometric and mechanical alignment tolerances, and is accurate only to the extent that the paraboloid vertex is mechanically centered on the mirror perimeter.

The secondary is inserted and centered mechanically on the alignment telescope axis with respect to its outer perimeter. The illuminated cross-hair in the eyepiece of the alignment telescope is viewed in reflection via the secondary, and the secondary is tilted until the image of the cross-hair is centered on the alignment telescope's axis. This action makes the secondary perpendicular to the axis at the point where the axis intersects its surface. The alignment telescope is removed.

B. Interferometric Alignment

The interferometric alignment procedure essentially consists of adjusting a small laboratory Michelson plane-wave interferometer, with a flat mirror in one arm and one of the telescope–siderostat systems in the other arm. The interferometer is illuminated by a helium–neon (0.633-μm wavelength) laser with a coherence length greater than ~60 m. One generates the expanded laser beam by focusing the laser output on a pinhole, allowing the diffraction-limited

beam to expand and fill a lens of ~5-cm diameter at a distance of one focal length, such that a parallel beam is generated. The beam is projected into the laboratory Michelson interferometer. The relay optics of the IOTA interferometer are arranged such that the light in one arm travels out from the laboratory to the telescope, expands to fill the primary mirror, reflects from the siderostat mirror back to the primary and secondary, and travels back into the laboratory, where the beam strikes the beam combiner and is interfered with the plane wave from the other arm of the interferometer.

The test beam thus double-passes all the optics from the beam splitter to the telescope, except for the siderostat mirror, which is only single-passed. The resultant interference pattern is displayed on a white card and monitored visually. This pattern is a function of any distortion in the wave front that is due to position errors of curved optical elements, flatness errors of the optical surfaces, and refractive fluctuations in the air-filled portions of the path.

If we can relate the observed fringes to specific misalignments of the telescope, we shall in principle be able to eliminate the misalignment by adjusting the positions of the telescope mirrors until the fringe pattern is reduced to a uniform field with zero fringes. Relating the observed fringes to specific misalignments was our motivation for doing the simulations in this paper.

In practice we align under conditions in which the major part (~80%) of the optical path is evacuated, eliminating a major disturbance. We do this on a cloudy day or at night well after sunset, to reduce convective air perturbations in the telescope shelter building, where essentially all the air path refractive perturbations occur. We find that the major impediments to alignment are the residual surface errors of the optical chain that are due to polishing or mounting distortions, and the turbulence in the telescope shelter. (An additional nonfundamental impediment is the particular design of our secondary-mirror supports, which makes some types of adjustment awkward; this deficiency will be remedied in a new five-axis secondary support that we are currently implementing.) A typical alignment procedure takes several hours per telescope and is limited by our ability to mentally subtract from the observed pattern the fixed pattern noise of the residual surface errors and the slow churning of the air in the telescope shelter, all of which add up to an estimated one wave peak to valley of background pattern in double pass.

3. Simulation Program

To perform our simulation we make use of two computer programs. The first one, RayTrace,[6] originally created to analyze the POINTS (precision optical interferometer in space) optical system, propagates a grid of pencil rays through the optical system with sufficient accuracy that the optical path length of each ray can be used to calculate the wave-front distortion at any point in the system. The output provides a matrix of parameters that describe the wave front.

The second program, IOTA_misalignment,[7] uses this matrix of parameters as input to compute the aberrated wave front and the interferogram pattern. The program produces plots of the interference patterns formed by the perturbed beam and the plane reference beam and plots of the intensity distribution of the beam without the presence of the reference beam.

The quantity of interest for our analysis is the variation in the shape of the wave front W as a function of any adjustment parameter Δ such as the position or tilt of a single component. Here W is the difference between the computed wave front and a perfect plane wave front, i.e., the wave-front distortion. For each point (ξ, η) in the end plane of the model optical system, typically a plane at the exit of the system near the primary mirror, W is calculated as

$$\begin{aligned} W(\xi, \eta) = {} & A_1 + A_2\xi + A_3\eta + A_4(\xi^2 + \eta^2) + A_5(\xi^2 + \eta^2)^2 \\ & + A_6(\xi^2 - \eta^2) + A_7\xi\eta + A_8(\xi^2 + \eta^2)\xi \\ & + A_9(\xi^2 + \eta^2)\eta + A_{10}\xi^3 + A_{11}\eta^3 \\ & + A_{12}(\xi^2 + \eta^2)(\xi^2 - \eta^2) + A_{13}(\xi^2 + \eta^2)\xi\eta \\ & + A_{14}(\xi^2 + \eta^2)^2\xi + A_{15}(\xi^2 + \eta^2)^2\eta \\ & + A_{16}(\xi^2 + \eta^2)^3. \end{aligned} \tag{4}$$

The aberration coefficients A_i $(i = 1, 16)$ specify the shape of the wave front in terms of piston (A_1), tip–tilt (A_2, A_3), defocus (A_4), and higher terms. A_i are generated in the program IOTA_misalignment according to the Taylor series

$$A_i = a_{i0} + a_{i1}\Delta + a_{i2}\Delta^2 + a_{i3}\Delta^3, \tag{5}$$

where the a_{ij} are the output parameters calculated in the program RayTrace and Δ is the magnitude of the input parameter that specifies the actual perturbation (i.e., a translation or a rotation) that we want to simulate.

A. Interference Pattern

The relative intensity pattern that results from the interference of the two wave fronts is given by

$$f(\xi, \eta) = 1 + \sin[2\pi W(\xi, \eta)/\lambda], \tag{6}$$

which is plotted by means of appropriate imaging graphics routines.

For each simulated perturbation the program also calculates the wave-front optical path variance δ^2. To evaluate the mean deviation of the calculated wave front from a plane, we need the best fit plane $p(\xi, \eta)$ to the aberrated wave front, which is given by the first three terms in Eq. (4):

$$p(\xi, \eta) = A_1 + A_2\xi + A_3\eta. \tag{7}$$

By subtracting Eq. (7) from Eq. (4) we get, at each point, the departure $q(\xi, \eta)$ from the best fit plane wave:

$$q(\xi, \eta) = W(\xi, \eta) - p(\xi, \eta). \quad (8)$$

The path variance δ^2 of the wave front is

$$\delta^2 = \sum_{i=1}^{N} q_i^2(\xi, \eta)/(N - 3), \quad (9)$$

where N is the number of points across the beam, typically $\sim 10^4$ in our simulations.

B. Intensity Pattern

To compute the position (X, Y) of the beam as it is seen in the laboratory one propagates each ray of the beam from the end plane to the laboratory according to

$$(X, Y) = (\xi - Z \times \partial W/\partial\xi, \eta - Z \times \partial W/\partial\eta), \quad (10)$$

where Z is the distance from the primary mirror's focal point to the laboratory optical display surface, which for the IOTA interferometer is typically $Z \sim 40$ m.

A large value of Z is an advantage here because any local wave-front curvature in the (ξ, η) plane tends to generate significant changes in the transverse distance between rays in the (X, Y) plane, thereby changing the electric field amplitude and the observed intensity. Departures from a uniform-intensity beam are clear signs of wave-front aberrations. These patterns were calculated[7] but are not included in the present paper; however, in practice the intensity pattern is nearly as sensitive as the interferogram pattern, and it is a reliable initial guide to aligning a telescope in this context.

4. Simulation Results

Here we analyze several possible initial telescope configurations and a set of perturbations to these configurations. Our goal in this section is to generate visual impressions of the types of laser autocollimation interferogram patterns that might be seen in the process of aligning an IOTA telescope at the interferometric level of accuracy.

We use the beam-compressor parameters given in Section 2. Although the analysis is specific to the IOTA interferometer, the method can be applied to any similar interferometer.

We use a conventional $(\hat{x}, \hat{y}, \hat{z}, \hat{\theta})$ coordinate system, where $\hat{z}$ is the unit vector along the intended symmetry axis of the telescope, $\hat{x}$ and $\hat{y}$ are the transverse perpendicular axes, and $\hat{\theta}$ is the tilt direction with respect to $\hat{z}$; azimuthal rotations about $\hat{z}$ have no effect on the results in this paper and are ignored. We use (x, y, z, θ) to represent mirror displacements from their ideal positions.

A. Secondary Offset and Tilt

Simulations were performed with a transverse offset x and a tilt θ of the secondary mirror. Offsets were in the range 1–100 μm, and tilts were either 0 or $\theta_\perp$, where

$$\theta_\perp = x/2f \quad (11)$$

is the tilt that, in the case of a paraboloidal mirror, compensates for an x offset in the paraxial approximation (see Fig. 1).

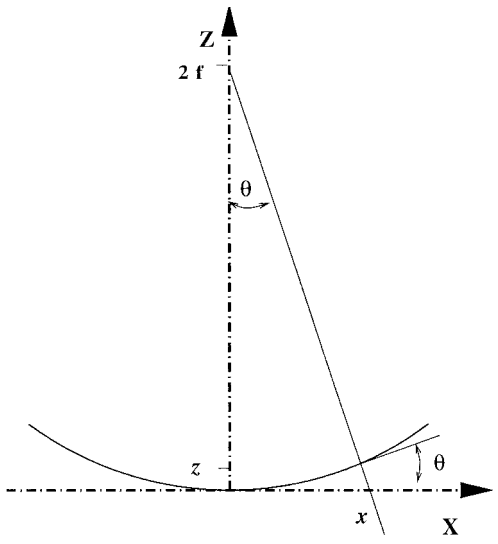

Fig. 1. Cross section of a paraboloidal surface and definition of $\theta_\perp$. Given a parabola $z = kx^2$, at any point (x, z) the slope is $\tan\theta = 2kx$, where $k = 1/(4f)$ and f is the focal length. For a ray parallel to the axis, a rotation of the mirror about its vertex by an angle θ is equivalent to a lateral shift of the mirror (in the paraxial approximation) by $x = 2f\theta$ and vice versa.

When $x \neq 0$ and $\theta = 0$, approximately straight fringes appear in the (X, Y) plane. Their number increases linearly to approximately 11 for $x = 10$ μm. When $\theta = \theta_\perp$ and $x < 10$ μm, no significant aberrations are observed (i.e., the rms is less than 0.1 μm). For $x \geq 30$ μm, coma and other wave-front errors, which are negligible for small displacements, show up, even when $\theta = \theta_\perp$ (cf. Subsection 5.D below).

Assuming that the primary mirror and the flat are perfectly aligned, if we detect fewer than ~ 11 fringes we infer that the secondary mirror is transversely displaced by less than 10 μm. By tilting the secondary mirror both clockwise and counterclockwise and observing the number of fringes, we can learn about the direction of the mirror displacement. If more than 11 fringes are detected, we infer that the displacement is larger than 10 μm, and with a proper tilt of the mirror we can almost eliminate them. However, in this case we should first correct for the lateral position of the mirror.

B. Secondary Offset and Focus

Several sets of computed interferograms were obtained by use of different combinations of transverse offset (x) and longitudinal focus (z) displacements, with fixed tilt $(\theta = 0)$ of the secondary mirror. Here we consider $x = 1$ μm and a z range from -40 to $+40$ μm and assume that the primary mirror and the flat

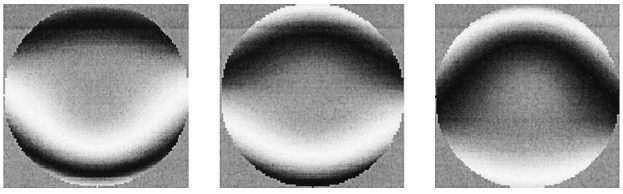

Fig. 2. Eyeball feature. The primary mirror and the siderostat are aligned, and the secondary mirror is transversely displaced ($x = 275$ μm) and tilted ($\theta_\perp = 1201$ μrad). Simulated interferograms are shown for an axial displacement of the secondary mirror to $z = -5$ μm (left), $z = 0$ μm (center), and $z = +5$ μm (right).

are perfectly aligned. When $z = 0$ the interferogram shows one fringe parallel to the y axis, which is due to the tilt of the wave front caused by the mirror's transverse shift. Moving the secondary mirror either toward or away from the primary mirror causes the fringes to become curved and, starting from $z = 20$ μm, their number increases noticeably. We also noted the appearance of a characteristic feature, which we named the eyeball feature, which changes position according to the sense of the transverse displacement. An example of this feature is shown in Fig. 2. Moving the mirror back and forward along the z axis, going through the focus point (the position of the secondary mirror for which the focal points of the primary and the secondary mirrors are perfectly coincident), causes the eyeball to appear at the bottom of the interferogram figure; then the fringes become increasingly straighter as the mirror approaches the focus point and start curving again but with opposite curvature, and the eyeball appears at the top of the figure. This trend is observed for all the transverse displacements considered, although the characteristic eyeball becomes evident at different values of z. This is so because the number of fringes increases proportionally both to x and to z and by different factors.

In the paraxial approximation, one can show[7] that for an afocal system the maximum wave-front errors in the $\hat{x}$ and the $\hat{z}$ directions, w_x and w_z, respectively, are given by

$$w_x = 2x/f_\#, \qquad w_z = z/4f_\#^2, \tag{12}$$

so the ratio of the wave-front errors in the two directions is

$$w_x/w_z = 8f_\# x/z. \tag{13}$$

Inasmuch as the number of fringes is given by w/λ, to get the same number of fringes either by an x displacement or by a z translation we must have $z = 8f_\# x$. For the IOTA interferometer with $x = 1$ and $z = 40$ μm we get two fringes shifted with respect to the center of the interferogram: The two fringes are due to the defocus error, whereas the shift is due to the mirror's transverse displacement. From a comparison of several cases, we also notice that the eyeball shows up at larger z for larger x and also that, with x kept fixed, the more z increases, the more difficult it is to detect the eyeball asymmetry, so for $w_z > w_x$ it eventually disappears. As a general rule of thumb we can expect to see the eyeball feature when defocus becomes the major cause of wave-front distortion, but the effect of transverse displacement is not negligible yet, i.e., $z \geq 8f_\# x$.

As x gets larger, the interferograms get less clear, but the eyeball can still be observed. This feature can be used as a sign to detect the transverse misalignment of the secondary mirror because if the mirror were aligned along the axis of the primary the fringes would be concentric to the center of the figure. One can evaluate the magnitude of the misalignment by counting the number of fringes when the mirror passes through the focus position.

C. Secondary Offset, Tilt, and Focus

For the set of simulations secondary offset, tilt, and focus the secondary mirror is transversely offset by x, tilted by the corresponding angle $\theta_\perp$, and moved along the z axis. For small lateral offsets the fringes observed when the secondary mirror is moved back and forward from the focal point resemble rather well those obtained when the mirror is on axis. However, starting from $x = 30$ μm, and for focus shifts within approximately $|z| < 10$ μm, the fringes are no longer concentric with the center of the interferogram. From back to front passing through the focus position, the asymmetry moves from the bottom to the top of the figure (Fig. 2). The observed asymmetrical feature is caused by the combination of defocus with the residual aberration as a result of the transverse displacement that the tilt correction has not removed.

Because by moving the mirror out of the focus position we observe similar interferogram features both when the secondary mirror is merely displaced and when it is displaced and tilted, we may wonder how we can discriminate between the two situations. One experimental procedure that we suggest is the following: If the mirror is just shifted, we expect to see the eyeball when x is small, i.e., less than 4–5 μm. By adjusting the transverse position by a few micrometers we should be able to place the mirror on axis. At this point, for any focus translation, no asymmetry should be observed and, when we move the mirror through the focus position, the fringes should disappear.

On the other hand, when x is quite large the parallel fringes that are due to the wave-front tilt prevail, and we should first correct for the large lateral shift. If the mirror were affected by both offset and tilt, adjusting its position by few micrometers along the x axis would not remove the asymmetry in the interferogram, and fringes would still be observed even when we move the mirror through the focus position.

D. Telescope Aligned but Tilted Off Axis

So far we have considered only misalignments of the secondary mirror, and we have implicitly assumed that the primary mirror was aligned along the focal axis of the system. However, mainly because of uncertainty in the position of the center of the primary mirror, the telescope alignment operation may result in a configuration in which the primary mirror is either transversely offset or tilted off axis, and con-

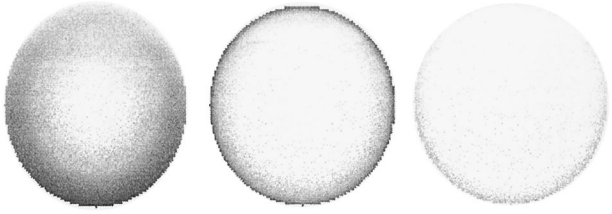

Fig. 3. Source off axis by an angle $\theta = 1200$ μrad. Interferograms with the system perfectly aligned (center) and with the secondary mirror displaced along the z axis by $z_s = -5$ μm (left) and $z_s = +5$ μm (right).

sequently the secondary mirror's position is adjusted until its misalignments correct for the effects that are due to the primary mirror's displacement. Thus essentially the primary and the secondary are aligned along an axis that is not parallel to the viewing axis; i.e., the telescope is being operated off axis.

The paraboloid–paraboloid system is tolerant of off-axis operation so long as the relative alignment of the primary and the secondary is maintained. For example, we show in Fig. 3 interferograms obtained with a perfectly aligned telescope used off axis (central interferogram) and with the secondary mirror displaced to $z = -5$ μm (left) and to $z = +5$ μm (right). The off-axis angle is 1200 μrad, and we notice that the positive defocus of the secondary reduces the wave-front error (see also Subsection 5.G and Fig. 4 below), so the Strehl ratio in the visible is of the order of 0.93. This demonstrates graphically that a large off-axis angle can be tolerated.

5. Alignment Tolerance

In this section we give results for the wave-front rms δ for several specific cases of misalignment of an IOTA telescope. The numerical results are helpful for gauging the accuracy with which the primary and the secondary mirrors must be adjusted. Each telescope mirror adjustment mechanism at the IOTA telescope is designed to have a sufficiently fine resolution that the requirements in this section can be met easily, and from experience we believe that the long-term stability of the adjustments is also within these requirements. The main issue, as discussed in this paper, is that of actually finding the optimum settings, particularly in the presence of other sources of wave-front distortion such as nonflatness of relay optics and turbulence in the air-filled part of the optical path.

For each type of alignment error we give the wave-front rms δ as a function of an offset or of an angle in units of meters or radians, respectively. The units of the constants in the relations to calculate δ vary according to the alignment perturbation considered. The results in this section refer to the case of the IOTA telescope in single pass, i.e., observing a star.

In addition, for each case we apply the criterion that $\delta = \lambda/20$ or less, corresponding to a Strehl ratio of ~0.91. This provides a limit on the excursion of the relevant adjustment parameter with respect to a perfectly aligned system, information that is of direct use in the adjustment process. Explicit parameter tolerance limits are presented for the R-band wavelength (0.70 μm). Key relations and results from this section are collected in Table 1.

A. Secondary Defocus

If an afocal telescope is perfectly adjusted except for an axial shift of magnitude z_s of the secondary, then it is relatively straightforward to show that the wave-front rms is given by

$$\delta = z_s/(16\sqrt{3}f_{\#}^2), \tag{14}$$

so for the IOTA telescope we get $\delta \simeq z_s/170$. We verified this relation numerically by running the simulation program; we obtained all other relations in this section by running the simulation and fitting an appropriate empirical function to the results.

Applying the $\lambda/20$ limit, then, we find that $z_s = 8.5\lambda$ is the tolerance limit on the focus position of the secondary, or typically 6 μm in the R band. These relations and the others in this section are collected in Table 1; note that the numerical values in this

Table 1. Alignment Tolerances for Several Elements of the IOTA Telescopes[a]

Subsection of This Paper	Type of Perturbation	Wavefront rms, δ	Parameter	
			for $\delta = \lambda/20$	for R Band
5.A	Secondary defocus	$z_s/170$	$z_s = 8.5\lambda$	$z_s = 6$ μm
5.B	Secondary shift	$x_s/2500$	$x_s = 125\lambda$	$x_s = 90$ μm
5.C	Secondary tilt	$\theta_s/25{,}000$[b]	$\theta_s = 1250\lambda$[b]	$\theta_s = 0.9$ mrad
5.D	Secondary shift and tilt	$x_s/5600$	$x_s = 280\lambda$	$x_s = 200$ μm
5.E	Primary shift and tilt plus secondary shift and tilt	$x_p/12{,}500$	$x_p = 625\lambda$	$x_p = 440$ μm
5.F	Telescope tilt	$\theta^2/18$[c]	$\theta = 0.95\lambda^{1/2}$[d]	$\theta = 0.8$ mrad
				$\lvert x_p - x_s \rvert = 820$ μm

[a]For each type of perturbation listed in column 2, the wave-front rms δ is given in column 3 as a function of the relevant parameter, the resultant tolerance for the case of a $\lambda/20$ rms (equivalent to a Strehl ratio of 0.91) is given in column 4 as a function of wavelength (meter and radian units for the tolerances and accordingly for the constants), and the specific numerical result for the case of the R band is listed in column 5.

[b]Constant units: rad/m.

[c]Constant units: rad^2/m.

[d]Constant units: $\text{rad}/\text{m}^{1/2}$.

table are rounded to approximately two significant places only, as greater accuracy is not justified. The secondary adjustment mechanism, as well as the primary–secondary spacing, must be accurate at this level or better.

B. Secondary Shift

When the secondary is only transversely shifted by an amount x_s, the simulation program shows that the wave-front rms is

$$\delta \simeq x_s/2500, \tag{15}$$

for which the $\lambda/20$ limit gives $x_s = 125\lambda$, or ~90 μm in the R band.

C. Secondary Tilt

For a pure tilt of the secondary by an angle θ_s, the simulation gives a wave-front rms of

$$\delta \simeq \theta_s/(25{,}000 \text{ rad/m}). \tag{16}$$

The $\lambda/20$ criterion yields a tolerance limit $\theta_s = 1250\lambda$, which gives $\theta_s = 0.9$ mrad at R.

D. Secondary Shift and Tilt

Suppose that the secondary has a transverse shift x_s and a nominally compensating tilt $\theta_s = \theta_\perp = x_s/2f_s$, so the secondary is perpendicular to the intended axis at the point where its surface intersects the axis. It can be shown[7,8] that this configuration generates coma, because the condition for zero coma in a system in which the secondary is shifted is that the secondary be tilted by an angle that turns out to be just $2\theta_\perp$. The marginal ray of the $(x_s, \theta_\perp)$ system will be tilted by an angle $\theta_{\text{coma}} = 9m\theta_\perp/(16f_\#{}^2)$. The corresponding wave-front rms, with all the rays used, was calculated with the simulation program, yielding

$$\delta \simeq x_s/5600. \tag{17}$$

Using the $\lambda/20$ criterion, we find an allowable shift of $x_s = 280\lambda$, which in the R band is $x_s = 200$ μm.

E. Primary Shift and Tilt Compensated by Secondary Shift and Tilt

Suppose now that the primary has a transverse shift x_p and a nominally compensating tilt $\theta_p = \theta_\perp = x_p/2f_p$, so the primary is perpendicular to the intended axis at the point where its surface intersects the axis. We then shift[7] the secondary by $x_s = (1 + f_s/f_p)x_p/2$ and tilt it by $\theta_s = x_s/2f_s$ to align it along the primary axis. The result of the operation is that, although both mirrors are displaced with respect to the axis of the system, they are both perpendicular to the axis at the points where their surfaces intersect it. The wave-front rms from the simulation program is

$$\delta \simeq x_p/12{,}500. \tag{18}$$

The $\lambda/20$ criterion gives an allowable shift $x_p = 625\lambda$, which in the R band is $x_p = 440$ μm.

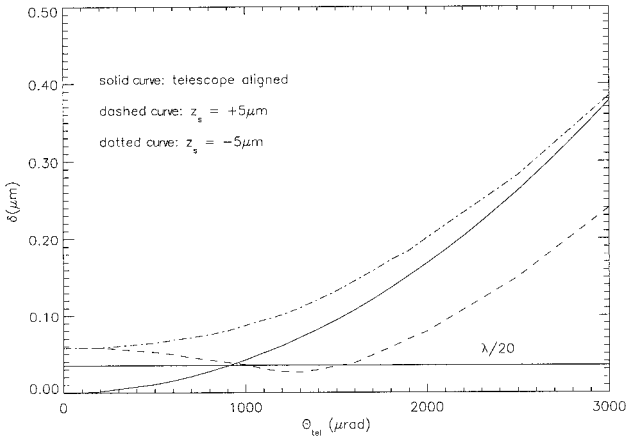

Fig. 4. Wave-front rms as a function of telescope tilt angle (or equivalently of star offset angle) when the telescope is perfectly aligned and when the secondary mirror is defocused by ±5 μm. The minimum rms achieved by a combination of telescope tilt and secondary defocus illustrates how the adjustment parameters can partially compensate for each other and also illustrates the fact that a minimum rms is not necessarily a sign of perfect adjustment. For reference, the $\lambda/20$ level is also shown. The plot is for single pass, i.e., viewing a star.

F. Telescope Tilt

An important property of an IOTA-like afocal telescope is that its spherical aberration, classic third-order coma, and astigmatism are all equal to zero.[8] Thus the system should work well even if it is tilted off axis. Although the alignment procedure would make it unlikely that the telescope would actually be perfectly aligned along an axis different from the target axis, it is nevertheless instructive to calculate the resultant aberration. Using the simulation program for a perfectly aligned telescope operated at an angle θ off axis, we find a quadratic dependence of

$$\delta \simeq \theta^2/(18 \text{ rad}^2/\text{m}), \tag{19}$$

where the units are meters and radians, respectively. Simulation results over a large range of angles θ are shown in Fig. 4 (solid curve); inspection of this figure shows that relation (19) holds near the axis and changes only modestly (to $\delta \simeq \theta^2/24$) for large angles ($\theta \sim 3000$ μrad).

The $\lambda/20$ criterion gives $\theta = 0.95\lambda^{1/2}$, or approximately $\theta = 0.8$ mrad. The corresponding difference in offset between the primary and secondary is $|x_p - x_s| = (f_p - f_s)\theta$, or 820 μm at the R band.

G. Telescope Tilt and Secondary Defocus

If both overall tilt and defocus are present, the combined effects can compensate for each other in a similar fashion to the way in which shift and tilt can compensate in either the primary or the secondary. However, with tilt and defocus the situation is more complex, as is shown in Fig. 4, where we show simulation results that give the wave-front rms δ as a function of the overall telescope tilt θ, or equivalently of the star offset angle, with superposed curves show-

ing the result of additionally shifting the secondary focus to $z_s = \pm 5$ μm. Note that for $z_s = +5$ μm the rms improves by approximately a factor of 2 for large tilt situations, showing that the aberrations can indeed partially compensate for each other's effects. An analysis of the outputs of the RayTrace program shows that the telescope tilt produces field curvature aberration, as shown in Fig. 3 (center). However, a simple translation of the secondary along the z axis also introduces field curvature, and we may expect that, depending on the direction of the translation, the wave-front rms will either improve or get worse. As the telescope tilt increases, the curve in Fig. 4 obtained with negative defocus shows that $\delta \sim \theta^2$, and this is due to the fact that the first three parameters a_{ij} [Eq. (5)] of the defocus coefficient A_4 are all positive. In the case of positive defocus the first and the third parameters of A_4 have opposite signs: When the contribution of the third term is comparable with that of the first term, the field curvature aberration decreases to a minimum value that corresponds to the minimum in the rms curve. From this point on, the contribution of the third parameter prevails, and the field curvature coefficient starts increasing as θ^2, and $\delta \sim \theta^2$ as in the cases of negative and no defocus. The plot is shown for a single pass, i.e., viewing a star, and the $\lambda/20$ criterion line is added to indicate the scale for the R band.

6. Expected Strehl Ratios

Here we evaluate the expected values of eight of the Strehl ratios listed in Section 1. Anticipating the results, we approximately rank-order these Strehl ratios from small to large, the same order as in Eq. (3), so the most critical ones are discussed first.

For comparison with observations (cf. Section 7 below), we evaluate the expected Strehl ratios for two representative wavelength bands, R (0.70 μm) and K (2.2 μm), although we note that the IOTA interferometer is operated over the full range of wavelengths *VRIJHKLM*. The results of this section are collected in Table 2.

For the *VRI* bands, where the telescope diameter is significantly larger than the Fried length r_0, we use a mask just before the beam combiner to effectively create four subapertures in parallel, each with a projected diameter of 0.16 m. With four parallel beams incident upon either side of the beam combiner, we have eight output beams; using lenses and weak prisms, we focus on eight separate areas of a CCD detector. For all other wavelength bands we use the full effective aperture.

A. Atmospheric Distortion Strehl Ratio S_{atm}

The atmosphere induces both tilt and curvature in a stellar wave front, as calculated, for example, by Noll.[9] When tilt is perfectly removed, the remaining wave-front distortion is characterized by a phase variance given by

$$\sigma^2 = 0.134[D/r_0(\lambda_0)]^{5/3}(\lambda_0/\lambda)^2, \qquad (20)$$

Table 2. Expected Strehl Ratios for Several Types of Perturbation

Subsection of this paper	Strehl Ratio Type	Strehl Ratio At R Band	Strehl Ratio At K Band
6.B	S_{servo}[a]	0.94	0.96
6.C	S_{flat}	0.65	0.96
6.D	S_{align}	0.96	0.99
6.E	S_{diff}	0.97	0.95
6.F	S_{flux}	0.98	0.98
6.G	S_{over}	0.99	0.99
6.H	S_{vib}	1.00	1.00
6.I	S_{win}	0.99	0.99
6.K	S_{inst}[b]	0.55	0.83

[a]For conditions of median seeing (0.7 arc sec) and a servo system matched to the atmospheric bandwidth.

[b]Expected overall instrument Strehl ratio from the product of rows 6.B–6.I.

where D is the telescope diameter and r_0 is the Fried parameter.

In principle, we can make seeing measurements at the IOTA interferometer directly from the star-tracker error signals, but we have not carried out a program to do this. However, we do know from the original site surveys at Mt. Hopkins that the IOTA site and the Multiple Mirror Telescope site have essentially identical seeing conditions,[10] at least to the accuracy of the method in use at the time (photographic trails of Polaris were recorded).

Seeing measurements are available from the Multiple Mirror Telescope,[11] in which a star was imaged with one of the Multiple Mirror Telescope's 1.8-m mirrors (telescope E) onto a CCD and the full width at half-maximum (FWHM) of the digitized video image was later extracted from the data. No guiding or tip–tilt correction was used. The measurements of interest here were recorded at the end of each night, over the period 11 October 1995 to 31 October 1996, after the installation of the rear shutter (which permits better ventilation of the dome volume). The median value of the 216 measurements is 0.70 arc sec FWHM, and very good seeing (i.e., best 10% of the measurements) is 0.44 arc sec FWHM. Using the relation[12] that seeing FWHM is given by λ/r_0, we find r_0 (median) = 0.16 m, and r_0 (very good) = 0.26 m.

In the R band we do not separately star-track each subaperture, so we do not expect the tilt removal to be as good as it could be; nevertheless the tilt will be substantially corrected frequently, so the present calculation should indicate the best that we can expect on those occasions, for which we use $D = 0.16$ m and find $S_{atm} = 0.92, 0.95$ at R for median and very good seeing, respectively. In the K band we use the full aperture and find $S_{atm} = 0.95, 0.97$ respectively (Table 3).

B. Star-Tracker Servo Time Constant Strehl Ratio S_{servo}

In a real star-tracker servo system there will always be a finite time delay after which the servo output will react to a previous input condition. This delay results

Table 3. Atmospheric and Servo Strehl Ratios for Two Seeing Conditions

Seeing (arc sec)	r_0 (λ_0) (m)[a]	S_{atm} At R Band	S_{atm} At K Band	S_{servo} At R Band	S_{servo} At K Band
0.70[b]	0.16	0.92	0.95	0.94	0.96
0.44[c]	0.26	0.96	0.98	0.97	0.98

[a] $\lambda_0 = 0.55$ μm.
[b] Median seeing.
[c] Very good seeing (best 10%).

from a combination of factors, including bandwidth in an analog system, sample interval time in a digital system, and finite slue time at the servoed mirror.

The effect of bandwidth in an ideal servo system has been modeled by Tango and Twiss,[13] who gave numerical results for the case when the bandwidth of the servo system is equal to the atmospheric cutoff frequency parameter (wind speed divided by πD) in Kolmogorov turbulence theory. We express their result as a phase variance σ^2_{servo}, where

$$\sigma^2_{servo} = 0.096[D/r_0(\lambda_0)]^{5/3}(\lambda_0/\lambda)^2, \quad (21)$$

which is similar in form to the result for atmospheric distortion. Using the same parameters as in the previous subsection, we find that $S_{servo}(R) = 0.94$, 0.96 for the R band with $D = 0.16$ m, and $S_{servo}(K) = 0.96$, 0.98 for the K band with $D = 0.45$ m, in conditions of median and very good seeing, respectively (Table 3).

In practice the IOTA's tip–tilt servo system operates at a selectable sampling frequency in a range of approximately 10–200 samples/s, depending on the brightness of the source. The correction is applied after a delay that is effectively approximately one half of a sample interval (10–0.5 ms), plus a delay for readout and centroid calculation (~0.5 ms) and an effective delay from the bandwidth-limited electronics (~1 ms), for a total delay of 11.5–2 ms. If this delay corresponds to ~1 rad or less of a servo system control frequency, the servo bandwidth will be at most 14–80 Hz. If the atmospheric cutoff frequency is of the order of 100 Hz, then clearly we are operating more slowly than in the ideal case. This suggests that we will experience an average loss that is greater than that in the ideal case calculated above, and such indeed is often the case.

However, for the purpose of comparison with the static Strehl ratios calculated in this paper, in Subsection 6.C we shall use only statistically selected visibilities near the top of an experimental distribution, so effectively we select those visibilities where the wave fronts are by chance nearly perfectly tilt corrected and only higher-order terms in the wave front are contributing to the visibility loss. This is approximately what is happening in an ideal servo system, so we retain the values calculated above for this analysis.

C. Flatness Strehl Ratio S_{flat}

The flatness Strehl ratio S_{flat} expresses the net result of figure errors in all the reflecting surfaces. The optical chain includes $N_s = 1$ siderostat mirror, $N_t = 2$ telescope mirrors, and typically $N_r = 11$ relay flats, including the beam splitter. We denote the wave-front rms from a typical mirror in each group by δ_s, δ_t, and δ_r respectively. We model the combined wave-front variance as the sum of the individual variances; this is equivalent to saying that a given ray traversing the system will experience random errors among the various surfaces and in particular that there is no correlation of surface errors among the mirrors. The total wave-front variance δ^2_{flat} from surface errors is then

$$\delta^2_{flat} = N_s\delta_s{}^2 + N_t\delta_t{}^2 + N_r\delta_r{}^2. \quad (22)$$

1. Siderostats

The siderostat mirrors were polished at Zygo Corporation to a specification that was $\lambda_l/6$ peak to valley (hereafter pv) surface error over the full clear aperture (a 0.43 m × 0.66 m inscribed ellipse) and $\lambda_l/20$ pv over any interior 0.13-m-diameter circle; the test laser wavelength was $\lambda_l = 0.633$ μm. Three such flats were polished; the average measured surface flatness was $\lambda_l/8.6$ pv and $\lambda_l/48$ rms, both over the full clear aperture. Several 0.13-m subapertures were measured on the third flat, giving an average result $\lambda_l/23$ pv. Clearly, the specifications were met and slightly exceeded. From the full aperture measurements we found that the average ratio of pv to rms is pv/rms ≃ 5.5, which we shall adopt as representative of all other optics in the chain. The wave-front rms is then

$$\delta_s = 2(\lambda_l/8.6)/[5.5\cos(30°)] \simeq \lambda_l/21, \quad (23)$$

where we adopt an average angle of incidence of 30° and the factor of 2 converts surface pv into wave-front pv.

2. Telescope Mirrors

The first two telescope mirrors were polished by Fair Optical Company to a specification on the assembled telescope that was $\lambda_l/3$ wave-front pv over 90% of the full aperture and $\lambda_l/10$ over any 0.15-m-diameter circular patch with the center on a 0.25-m diameter circle. Knife-edge testing, plus photographic interferograms of the primary alone and also of the assembled telescope, suggests that these specifications were indeed met, although no quantitative measurements were performed. Allocating the wave-front error equally between the two mirrors and assuming normal incidence, we found

$$\delta_t = \lambda_l/(3\sqrt{2})/5.5 \simeq \lambda_l/23 \quad (24)$$

for the wave-front rms from each telescope mirror.

3. Relay Mirrors

The flat relay mirrors were polished by Planar Optics, Inc., to a specification of $\lambda_l/20$ pv over the full

useful aperture. Photographic interferograms suggest that this specification was met and slightly exceeded. The average relay flat is used at an angle of incidence of 45°, so we found

$$\delta_r = 2(\lambda_l/20)/[5.5\cos(45°)] \simeq \lambda_l/39 \qquad (25)$$

for the wave-front rms from each relay mirror.

Combining the variances, we found the net wave-front rms to be

$$\delta_{\text{flat}} = \lambda_l/8.7 \simeq 0.073\ \mu\text{m} \qquad (26)$$

for the full optical chain. The corresponding Strehl ratios are $S_{\text{flat}} = 0.65$ at the R band and 0.96 at the K band.

We can, in principle, test the above calculation by measuring the observed wave-front variation when the interferometer is being aligned in autocollimation mode. Our visual impression is that there is an irreducible fringe pattern that remains after the available adjustments are made, and the magnitude of this pattern is roughly $1\lambda_l$ pv. For comparison, we can calculate an expected pv in double pass as $2 \times 5.5(\lambda_l/8.7) = 1.3\lambda_l$, which is of the order of $1\lambda_l$, suggesting that we have actually found the minimum rms and that the disagreement is due to lack of accuracy in our visual detection.

D. Alignment Strehl Ratio S_{align}

Let us suppose that in practice the primary and the secondary mirrors can be aligned to an accuracy that yields a double-pass laser-illuminated alignment interferogram in the lab that has an excursion of approximately 1/4 wave pv from the alignment process *per se*. We implicitly assume that the ten or so telescope adjustment parameters (tip, tilt, despace, etc.) do not represent as many independent degrees of freedom but are coupled in such a way that a minimum (but not necessarily unique) rms can be found experimentally.

Assuming that we are comparing the test beam with a flat reference beam in an interferometric arrangement, over the full aperture of the telescope the value 1/4 fringe pv in double pass corresponds to 1/8 wave pv in single pass, or a wave-front error of $\sim$1/32 wave rms, conservatively assuming that there is approximately a factor of 4 relating rms to pv.

The expected wave-front rms from the alignment procedure is then

$$\delta = \lambda_l/32 = 0.020\ \mu\text{m}. \qquad (27)$$

We assume that this number will not scale with the aperture diameter, because, for at least one kind of alignment error, a curvature across the full aperture, the subapertures are likely to see approximately the same pv excursion as the full aperture. (On the other hand, for a simple tilt error the subapertures will see a pv excursion that does scale as the subaperture diameter.) So, assuming no scaling, the Strehl ratio will be $S_{\text{align}} = 0.968$ at R and 0.997 at K.

E. Diffraction Strehl Ratio S_{diff}

Diffraction effects have been studied by Tango and Twiss[14] for the general case of a two-aperture system, and exact results have been tabulated in terms of parameters that are functions of wavelength, aperture diameter, and distance from the aperture to the beam combiner. The tabulated results have not been parameterized for simple display, but it is worth noting that for the full range of conditions considered by Tango and Twiss the calculated Strehl ratio is always in the range 0.87–1.00, so fortunately diffraction should never be a major effect for the IOTA interferometer. However, it is possible that atmospheric turbulence combined with large magnification factors and long paths could conspire to generate folded or cusplike wave fronts at the beam combiner, as studied by Bagnuolo,[15] but strictly speaking this is primarily a geometric effect, not a diffraction effect.

To apply the results of Tango and Twiss, one must select the diameter that is appropriate to the propagated beam in the interferometer, which here is the secondary mirror diameter. The diffraction Strehl ratio is unity if the propagation paths are equal, so we chose to evaluate the case in which the paths are relatively extreme in the IOTA interferometer, of the order of 40 m in one arm and 80 m in the other. The resultant Strehl ratios are $S_{\text{diff}} = 0.975$ at R and $S_{\text{dif}} = 0.95$ at K.

F. Flux Ratio Strehl Ratio S_{flux}

There are several ways in which the intensities of the combined beams in an interferometer might have unequal intensities but still be perfectly overlapped: The telescope diameters might be different, the relay optics might have different transmission factors, or the beam combiner might have unequal reflection and transmission coefficients. Suppose that the intensity ratio at the beam combiner is given by r. Then a straightforward calculation shows that the Strehl ratio is given by

$$S_{\text{flux}} = 2/(r^{1/2} + r^{-1/2}). \qquad (28)$$

We chose a moderately extreme value of $r \simeq 2/3$ and found that $S_{\text{flux}} = 0.980$.

G. Image Overlap Strehl Ratio S_{over}

The image overlap Strehl factor S_{over} describes the effect of a constant wave-front tilt from one telescope with respect to another, as could be generated by an initial error in setting up the star-tracker target points.

In practice with the IOTA system at the beginning of the evening, but after thermal stability has been achieved (roughly 1 h after sunset), we nominally acquire a target star with each telescope's star tracker. We then combine the parallel beams at the beam combiner and view the star images by means of a flip-in mirror, using a CCD camera with 0.6-arc sec pixels. (Before September 1998 this was done visually and probably less accurately.) The integration time of the CCD is in the approximate range 0.1–6 s, depending on the brightness of the star. By shuttering one beam and viewing the star image of the

other, we can determine the centroid of one time-averaged image to an accuracy of ~0.02 arc sec on the sky. The second image is then viewed and its centroid found. The second beam is tilted and remeasured iteratively until its position agrees with that of the first. The net result is that the wave fronts are parallel to within ~0.03 arc sec. With our current degree of temperature control in the beam-combining area we find that the image positions remain stable all night near this level, but for the purpose of the present paper we assume that some drift takes place and that for the average observation the two beams overlap with a relative angle of ~0.05 arc sec.

A straightforward calculation of the fringe amplitude in an interferometer in which the beams are combined at an angle θ shows that the modulation from this effect is given by

$$S_{\text{over}} = 2J_1(\pi D\theta/\lambda)/(\pi D\theta/\lambda) \simeq 1 - (\pi D\theta/\lambda)^2/8 + \ldots, \tag{29}$$

where D is the telescope diameter and θ is the angle between wave fronts projected on the sky. This result provides us with an overlap criterion in the form

$$\theta = 2\sqrt{2}\lambda\sqrt{\Delta S}/\pi D \simeq 0.285\lambda/D, \tag{30}$$

where the numerical value is for a 10% drop in S.

For the R band and a 0.16-m subaperture we find $S_{\text{over}} = 0.996$, and for the K band with a 0.45-m aperture we have $S_{\text{over}} = 0.997$.

H. Vibration Strehl Ratio S_{vib}

Vibration effects are extremely small in the IOTA system. Here we list the three instances in which vibration was detected and what was done to eliminate the effect. The net result is that we believe the vibration to be so small at the IOTA interferometer that $S_{\text{vib}} = 1.00$ is an appropriate expectation value.

1. *Vacuum Pumps*

In 1994, before beginning observations with the IOTA system, we found that the vacuum pumps vibrated the ground sufficiently that fringes from a laboratory mercury lamp in double pass (autocollimation) were sometimes blurred just enough to reduce their visibility substantially but not to zero, suggesting that the path variation in single pass was approximately one wavelength in double pass. If the modulation is sinusoidal, then the rms path variation in single pass is smaller by a factor $4\sqrt{2}$, so $\delta = 0.097$ μm. We then mounted the pumps on a massive concrete platform isolated from the ground by springs, obtaining a system with a resonant frequency of ~1.6 Hz and providing an isolation factor of $1/[(30/1.6)^2 - 1]$ or 1/350. The resultant Strehl ratio is well in excess of 0.999.

2. *Tip–Tilt Mirror*

No further vibrations were seen until we began operations with the K-band single-mode fiber beam combiner[16] approximately 2 years later. The improved visibility accuracy that is achievable with the fiber system allowed us to detect a small modulation of the star signal that was generated by ringing of the star-tracker tip–tilt mirror when the mirror was commanded by each new sample; the feedback circuit bandwidth of ~10 kHz was reduced to less than 1 kHz, and the ringing stopped, as expected.

3. *Mirror Carriage*

Recently the single-mode fiber beam combiner, operating in the thermal infrared at the L band, uncovered another square-wave vibration, probably caused by tipping of the moving mirror carriage when the normal smooth acceleration commands were temporarily replaced by square-wave changes in commanded position, in a repetitious fashion. We believe that the square-wave driving waveform edges caused the carriage to tilt, and a slightly different thermal background to be seen, causing the signal fluctuation. The solution is to drive the carriage smoothly, as is done in all cases but this one.

I. Window Strehl Ratio S_{win}

The vacuum windows used in the IOTA interferometer for the *VRIJHK* bands are 7.62 cm in diameter by 1.27-cm-thick Infrasil 301 from Heraeus Amersil, Inc. The specifications for index-of-refraction variation are $\Delta n \leq 2 \times 10^{-6}$ pv over 80% of the clear aperture, a flatness of $\lambda_l/20$ pv, and parallel to 0.0013 cm. The index specification gives a Strehl ratio of 0.994 at the R band for two windows in series, which is a negligible perturbation. The Strehl ratio at the K band is likely closer to unity, but without further information we shall take it to be the same as at the R band. The windows for the *LM* bands are BaF_2, but treatment of these wavelengths is outside the scope of this paper.

J. Polarization Strehl Ratio S_{pol}

Polarization is potentially a significant source of visibility loss, as was first pointed out by Traub,[17] who also suggested a way to eliminate polarization effects by making the mirrors at each stage of reflection in the two arms have the same type of reflecting surface and the same orientation. This direction cosine rule ensures that the s and the p polarizations experience the same shifts in both arms and therefore interfere with the same visibility pattern at the beam splitter. With the IOTA interferometer we do follow the direction cosine rule, except for the symmetry-breaking beam combiner surface, but we do not have a complete set of measurements of the polarization properties of the mirrors or transmitted beams and so cannot evaluate this term.

K. Expected Strehl Ratio S_{inst}

The results of Subsections 6.B–6.I are summarized in Table 2, where we have conservatively rounded down each entry to just two significant figures and for S_{servo} we assumed median seeing and a servo speed appropriate to the atmospheric conditions (i.e., a nominally ideal case). The product of these eight terms is $S_{\text{ins}} = 0.55$ in the R band and $S_{\text{ins}} = 0.83$ in the K

band. In Section 7 we compare these expected values with observations at the IOTA interferometer.

7. Measured Visibilities

We compare the expected instrumental visibilities listed in Table 2 with the observed visibilities of the IOTA interferometer in the following way: We typically measure several hundred visibilities in a few minutes of observation and form a frequency distribution histogram. The atmospheric perturbations generate a distribution that is biased toward visibilities that are almost always smaller than those that are due to the instrument plus object alone.

The shape of the visibility distribution and the analysis of this shape for the purpose of deriving unbiased estimates of object visibilities are not elaborated here. In short, however, we believe that the observed spread in visibilities is due primarily to a combination of effects, including scanning somewhat more slowly than the atmospheric coherence time, which causes interferograms to be distorted in midscan, and the finite reaction time of our tip–tilt servo, which is less than ideal, as discussed in this paper.

Thus, to isolate the instrumental contribution, we look at the upper end of this distribution and observe only pointlike sources. We have done this for a representative subset of data obtained with the IOTA system. We define the quantity $V_{\mathrm{meas}}^{\mathrm{top}}$ as the median value of the upper 10% of visibilities in a measured distribution; the value of 10% is large enough to give a statistically significant sample but still small enough to represent the population of essentially unperturbed wave fronts.

In addition, each data set was screened with a battery of statistical tests to eliminate outliers. These tests were designed to reject obviously bad data points, such as might be caused by an occasional instrument malfunction. One test searches for cosmic ray hits on the detector, which show up as large, single glitches. Another test examines the trend of interferogram centroid (or delay) values and rejects those that lie more than three standard deviations away from the linear trend; for example, if the interferogram fell partially outside the scan window, it might generate such an outlier point. Another test rejects visibilities that are smaller than three times the rms noise value in the noninterferogram part of the scan, thus eliminating low signal-to-noise values that might in fact be pure noise. Another test rejects visibilities larger than unity, which are in principle possible in a well-aligned system in the presence of photon noise, for example, but which in practice we do not expect to see.

In the R band we found the median of the upper 10% of the combined data from all four parallel channels to be $V_{\mathrm{meas}}^{\mathrm{top}} = 0.49 \pm 0.05$ on a night when the atmospheric seeing was relatively good and the instrument was well aligned; the individual channel medians were 0.54 ± 0.02, 0.53 ± 0.01, 0.46 ± 0.09, 0.45 ± 0.09, respectively, showing that the different channels show characteristically biased visibilities. Experience and experimentation clearly show that these biases are the result of small changes in the alignment and the accuracy of parallelism of the wave fronts. On other nights we observed both larger (occasionally) and smaller (frequently) values of instrumental visibility, and it is our experience that by far the most common cause of these different visibilities, apart from the dominant one of changes in atmospheric seeing, is the overlap accuracy of the star images; it rarely is the alignment of the telescope's curved optics. We note that the data cited here were obtained before the current CCD-based image overlap camera was installed, so the overlap was done by eye, which we believe gives lower average accuracy than overlap done with the camera.

Table 4. Estimated Net Strehl Ratio for Some Seeing Conditions and Measured Visibilities

		$S_{\mathrm{atm}} \times S_{\mathrm{inst}}$	
Seeing (arc sec)	r_0 (λ_0) (m)[a]	At R Band	At K Band
0.70[b]	0.16	0.51	0.79
0.44[c]	0.26	0.53	0.81
$V_{\mathrm{meas}}^{\mathrm{top}}$		$0.49 \pm .05$	$0.70 \pm .05$

[a] $\lambda_0 = 0.55$ μm.
[b] Median seeing.
[c] Very good seeing (best 10%).

By a similar process for data in the K band we found a measured instrumental visibility of the top 10% to be $V_{\mathrm{meas}}^{\mathrm{top}} = 0.70 \pm 0.05$, a value that varies less from night to night than those of visible band visibilities. (This value applies to the case of the classic Michelson beam combiner, not to the single-mode fiber optic beam combiner,[16] which has an effective instrumental visibility of the order of unity.)

We have collected results in Table 4. The first two rows contain the expected values of r_0 and $S_{\mathrm{atm}} \times S_{\mathrm{ins}}$ as calculated in Section 6. The third row contains the measured values of $V_{\mathrm{meas}}^{\mathrm{top}}$. Our method of presenting results in this paper essentially retains only those visibility values for which the bandwidth of the tip–tilt servo system matches that of the atmosphere, a state in which there is little loss from this part of the system. In practice we do not routinely achieve this condition. However, inasmuch as our primary purpose in this paper is to compare expected telescope errors (and other static errors) with observations, we believe that this procedure is easily justified.

From Table 4 we see that expected Strehl ratios are in fact close to the observed top visibilities and that they are within the uncertainties at the R band. At the R band we expect a Strehl ratio of 0.53 for very good seeing, and we measure 0.49 ± 0.05; at the K band we expect 0.81 for very good seeing, and we measure 0.70 ± 0.05. This result suggests that at the K band there are further visibility loss factors beyond those discussed here or that we have somewhat overestimated the relevant Strehl ratios.

Nevertheless, the agreement in the R band and the roughly nominal agreement in the K band are of value in showing that some degree of understanding exists, and, perhaps most important, the process of comparison provides a guide to possible future improvements that might be implemented.

8. Conclusions

We have shown how wave-front propagation in a stellar interferometer can be modeled and numerically simulated. We have given examples of the theoretical double-pass laser alignment interference patterns that are produced by several types of telescope alignment error and discussed how these errors can be detected and corrected.

We have shown graphically and algebraically the effects of telescope misalignment, and for various types of misalignment we have provided explicit estimates of the allowable adjustment tolerances. For perspective we also considered all other known sources of perturbation to the wave front and provided estimates of the resultant Strehl ratios.

We showed that the alignment of the afocal Cassegrain collecting telescopes used in the IOTA interferometer should be able to be carried out sufficiently accurately that any residual telescope alignment errors will be relatively small compared with three of the total of ten possible sources of fringe contrast loss. Our results suggest that the dominant sources of loss of coherence at the IOTA interferometer are the flatness of the optics, the uncompensated atmospheric wave-front perturbations, and the servo system time lag (for matched servo and atmospheric bandwidths), in that order and for the R band. For the K band these three sources introduce losses of the same order of magnitude. A slower servo system will further degrade performance.

We found, after allowing for the fact that the tip–tilt servo system is generally operated at a slower sampling speed than would be optimum, that the observed visibilities (visual, 0.49 ± 0.05; infrared, 0.70 ± 0.05) are somewhat lower than expected from our model (visual, 0.53; infrared, 0.81), by approximately 1 and 2 times the measurement uncertainty, respectively.

These values of instrumental visibility, along with the moderately good agreement between measurements and model, suggest that first, there is room for some improvement in our model, and second, that there is even more room for improvement in our experimental technique, but third, that the physical origin of the finite Strehl ratio in each IOTA subsystem is relatively well understood and, perhaps more important, the quantitative rank ordering of each subsystem's Strehl ratio can be used as a reliable guide in planning for future instrumental improvements.

I. L. Porro is grateful to the Smithsonian Institution for the award of a predoctoral fellowship for the years 1994 to 1997 and to P. L. Bernacca of the University of Padua for his encouragement. The research in this paper was supported in part by grants from the National Science Foundation and NASA (NAG 5-4900). We thank R. D. Reasenberg, M. A. Murison, and M. C. Noecker for their help with the development of the simulation program. We also thank R. Millan-Gabet and F. P. Schloerb for discussions regarding the visibility distribution function and M. G. Lacasse for valuable technical assistance during the observations with the IOTA interferometer. Finally, we thank two anonymous referees for their careful reading and constructive comments.

References

1. V. N. Mahajan, "Strehl ratio for primary aberrations: some analytical results for circular and annular pupils," J. Opt. Soc. Am. **72,** 1258–1266 (1982).
2. T. A. ten Brummelaar, W. G. Bagnuolo, and S. T. Ridgway, "Strehl ratio and visibility in long-baseline stellar interferometry," Opt. Lett. **20,** 251–256 (1995).
3. W. A. Traub, "Recent results from the IOTA interferometer," in *Astronomical Interferometry*, R. Reasenberg, ed., Proc. SPIE **3350,** 848–855 (1998).
4. N. P. Carleton, W. A. Traub, M. G. Lacasse, P. Nisenson, M. R. Pearlman, R. D. Reasenberg, X. Xu, C. M. Coldwell, A. Panasyuk, J. A. Benson, C. Papalislios, R. Predmore, F. P. Schloerb, H. M. Dyck, and D. M. Gibson, "Current status of the IOTA interferometer," in *Amplitude and Intensity Spatial Interferometry II*, J. B. Breckinridge, ed., Proc. SPIE **2200,** 152–165 (1994).
5. I. L. Porro, W. A. Traub, and N. P. Carleton, "Importance of telescope alignment for the performance of a stellar interferometer," in *Astronomical Interferometry*, R. Reasenberg, ed., Proc. SPIE **3350,** 414–423 (1998).
6. M. A. Murison, "Ray trace analysis of selected POINTS optical subsystems," Memo TM 93-07 (Smithsonian Astrophysical Observatory, Cambridge, Mass., 1993).
7. I. L. Porro, "A stellar interferometer on the Moon. An interdisciplinary analysis to determine the preliminary characteristics of the instrument, on the basis of the experience acquired with the IOTA interferometer," Ph.D. dissertation (University of Padua, Padua, Italy, 1996).
8. D. J. Schroeder, *Astronomical Optics* (Academic, San Diego, Calif., 1987).
9. R. J. Noll, "Zernike polynomials and atmospheric turbulence," J. Opt. Soc. Am **66,** 207–211 (1976).
10. M. R. Pearlman, D. Hogan, K. Goodwin, and D. Kurtenbach, "A meteorological report for the Mt. Hopkins observatory: 1968–1971," SAO Special Rep. 345 (Smithsonian Astrophysical Observatory, Cambridge, Mass., 1972).
11. C. Foltz, "Seeing improvements resulting from improved chamber ventilation," MMTO Conversion Tech. Memo. 96-4 (Multiple Mirror Telescope Observatory, University of Arizona, Tucson, Ariz., 1996).
12. A. Glindemann, "Beating the seeing limit—adaptive optics on large telescopes," *Habilitationsschrift* (Ruprecht-Karls-Universität Heidelberg, Heidelberg, Germany, 1997) Chap. 2, pp. 11–13; "Relevant parameters for tip-tilt systems on large telescopes," PASP **109,** 682–687 (1997).
13. W. J. Tango and R. Q. Twiss, "Michelson stellar interferometry," in *Progress in Optics*, E. Wolf, ed. (North Holland, Amsterdam, 1980), Vol. XVII, pp. 239–277.
14. W. J. Tango and R. Q. Twiss, "Diffraction effects in long path interferometers," Appl. Opt. **13,** 1814–1819 (1974).
15. W. G. Bagnuolo, "Simulations for the CHARA/GSU interferometer and binary star speckle photometry," in *High-Resolution Imaging by Interferometry*, F. Merkle, ed., Vol. 29 of ESO Conference and Workshop Proceedings (European Southern Observatory, Garching bei München, Germany, 1988), pp. 981–986.
16. V. Coudé du Foresto, G. Perrin, C. Ruilier, B. P. Mennesson, W. A. Traub, and M. G. Lacasse, "FLUOR fibered instrument at the IOTA interferometer," in *Astronomical Interferometry*, R. Reasenberg, ed., Proc. SPIE **3350,** 856–863 (1998).
17. W. A. Traub, "Polarization effects in stellar interferometers," in *High-Resolution Imaging by Interferometry*, F. Merkle, ed., Vol. 29 of ESO Conference and Workshop Proceedings (European Southern Observatory, Garching bei München, Germany, 1988), pp. 1029–1038.